Journal of
Materials Chemistry B

ROYAL SOCIETY
OF CHEMISTRY

PAPER

View Article Online
View Journal | View Issue

CrossMark
click for updates

Cite this: *J. Mater. Chem. B*, 2016, 4, 3998

Direct cellular organization with ring-shaped composite polymers and glass substrates for urethral sphincter tissue engineering†

Wenqiang Du, Jianfeng Chen, Huan Li, Gang Zhao,* Guangli Liu, Wulin Zhu, Dong Wu and Jiaru Chu

Received 20th February 2016,
Accepted 3rd May 2016

DOI: 10.1039/c6tb00437g

www.rsc.org/MaterialsB

Although fundamental efforts have been made to engineer circular smooth muscle layers *in vitro*, engineering structured skeletal muscle tissue equivalents acting as sphincters remains to be investigated. Groove patterned substrates made of homogeneous materials usually lead to cell monolayers instead of patterned cell sheets while patterned matrices failed to generate circular myotubes because cell chirality blocks the end-to-end cellular sequence corresponding to pattern directions. In this paper, we proposed concentric circular and elliptical microgroove patterned substrates with glass substrates as grooves and polymers as ridges to direct ring-shaped myoblast patterns and maximize cell alignment with respect to constraint directions, which are essential for circular myotube generation towards sphincter tissue engineering. Our results showed that our substrates direct myoblasts to proliferate in and orient along the directions of glass grooves, leading to a higher cell alignment degree than homogeneous substrates can achieve. We also found that the cell alignment degree depends on dimensions and parallelism rather than the curvature of the constraint. On the basis of these findings, we proposed finite element models that quantitatively account for our experimental data and emphasized the role of intercellular forces in cell alignment modulation. These results suggest that narrow curved constraints with parallel boundaries can favourably maximize myoblast alignment and facilitate myogenic differentiation regardless of constraint curvature, which will underpin the design of substrates and scaffolds for urethral sphincter or other hollow tissue engineering applications.

Introduction

Muscle tissues are vital for the movement and mechanical work of our body. Circular or elliptical muscle layers are widely observed *in vivo* and vital to many physiological processes. The architectural organization of these muscle cells, including cell patterns (spatial distribution of cells) and cell alignment, is crucial for the retention of muscle functions. For example, vascular smooth muscle cells are circumferentially aligned to provide blood vessels the strength properties for pulsatile blood flow. Circular skeletal muscles consist of concentric circular or elliptical arranged myofibers serving as sphincters to guard entrances and exits of the body by contraction and relaxation.

In vivo, loss of architectural organization of muscle cells causes diseases such as muscular dystrophy. Stress urinary incontinence (SUI) refers to the involuntary loss of urine under stress such as running and sneezing. The external urethral sphincter is a small circular skeletal muscle whose contractility is weakened while still functioning in most SUI patients. Damage of the architectural organization of external urethral sphincter cells caused by childbirth, surgical trauma and so forth is permanent.[1,2] Millions of people are affected and billions of US dollars are spent annually worldwide. The fact that the urethral skeletal muscle reduces rapidly with increasing age makes SUI a major issue to be addressed. Treatments of SUI through related muscle training, pharmaceutical injection, medical device installation and surgery only have limited effects and are probably associated with complications. Stem cell therapy for SUI has recently provided a promising option for SUI treatment *in vivo*. But unhealthy microenvironments inside SUI patients are possibly unable to provide sufficient differentiation and consequential cellular architectural organization cues for urethral sphincter regeneration.[3] Therefore, it is crucial to engineer the circular ring-shaped external urethral sphincter *in vitro*.[4]

In order to restore the circular external urethral sphincter *in vitro*, both cell patterns and cell alignment have to be engineered.

Department of Precision Machinery and Precision Instrumentation, University of Science and Technology of China, Hefei 230027, China. E-mail: fvc@ustc.edu.cn

† Electronic supplementary information (ESI) available. See DOI: 10.1039/c6tb00437g

Engineering ring-shaped cell patterns and maximizing cell alignment corresponding to cell patterns are vital to circular myotube generation and important stages of urethral sphincter engineering. The higher degree of cell alignment corresponding to ring-shaped cell patterns means a more end-to-end cellular sequence, which can facilitate myoblast fusion towards ring-shaped myotube generation. The state-of-the-art approaches to engineer cell patterns in two dimensions are usually accompanied by oriented cells. These approaches mainly include chemical cues such as surface matrix patterning.[5–9] However, physical cues such as topographical and mechanical simulations have been demonstrated to play a significant role that is superior to the patterned matrix in cell alignment regulation.[10–14] But with these physical features, a continuous cell monolayer instead of hollow cell patterns is usually obtained.[15–17] Alternative solutions have been developed by depositing smooth muscle cells on the inner surfaces of orthogonally microtextured hollow tubes. But it is difficult to precisely control the dimensions and shapes of the hollow structures,[18–21] which restrict their applications in tissue engineering. In addition, skeletal muscle cells are seldom studied on circular microtextured substrates or in tubes stated above because unlike circular smooth muscle layers, most of the circular skeletal muscles *in vivo* are macroscale structures except the urethral sphincter whose minimum diameter is about two millimetres.

In this paper, we aimed to engineer circular and elliptical ring-shaped cell patterns and maximize cell alignment corresponding to cell patterns for urethral sphincter engineering. In this scenario, dimensions and curvatures of circular constraints should be taken into consideration. Although myoblast behaviours under the influences of a circular ring-shaped matrix have been investigated, the width of the pattern was fixed.[22,23] Moreover, cells exhibit intrinsic chirality on the patterned matrix with circular boundaries which block the end-to-end cellular sequence with respect to the circular pattern.[22,24] Cells are badly oriented and circular myotubes can be hardly formed under this situation. Additionally, considering that the shape of the urethral sphincter *in vivo* is more like an elliptical than a circular ring, myoblast alignment under the influence of parallelism of the inner and outer boundaries of the constraint, which has not been considered in previous studies where constraints with parallel boundaries are used,[18–22] should also be investigated. For these purposes, glass substrates patterned with concentric circular (parallel) and elliptical (unparallel) polymeric microridges were presented. These substrates were designed to pattern cells and maximize cell alignment through combining the advantages of mechanical and topological cues in cellular organization regulation.

We find that dimensions and parallelism rather than the curvature of curved constraints profoundly affect myoblast alignment. To access the underlying mechanism of our experimental data, we also proposed finite element models and implemented the drug test and hence revealed the role of intercellular forces in cell alignment modulation. Myoblasts tend to align with the direction of maximum intercellular principal stress exerted by adjacent cells. The process can be strengthened by parallel while disturbed by unparallel boundaries of constraints. With these models, we also demonstrated why dimensions of constraints can substantially affect cell alignment while the curvature of constraints cannot and why cells exhibit position-dependent orientation behaviour with respect to boundaries of the constraint. Additionally, parallelism and dimensions of constraints also affect the differentiation of myotubes through altering the shape of myoblasts and their nuclei. Due to its simplicity of fabrication, our substrate provides an effective method to maximize curved myoblast alignment for circular myotube generation towards sphincter tissue engineering.

Materials and methods

Substrate fabrication

Substrates were fabricated by standard photolithography procedures. Briefly, coverslips (Citoglas, China), 20 mm × 20 mm × 0.17 mm, were pre-cleaned and dried before used. Then hexamethyldisilazane (HMDS, Sigma Aldrich, US) was spin coated on coverslips as the adhesive layer. An AR-P3540T photoresist (Allresist GmbH, Germany) was spin-coated, exposed with a mask under UV radiation for 10 s, developed in AR-P200 and then baked at 120 °C for 20 min. Substrates were then plated into 35 mm Petri dishes, sterilized and coated with 6 μg ml^{-1} of collagen rat tail, type I solution (Gibco, US) and sterilized again before used. An atomic force microscope (AFM) was used to measure the thickness of the coated collagen layer and the stiffness (Young's modulus) of the substrates.

Cell culture

C2C12 mouse myoblast cell lines (Cell Bank of Chinese Academy of Sciences, China) were cultured in Dulbecco's Modified Eagle Medium supplemented with 10% fetal bovine serum and 1% streptomycin/penicillin (Culture medium, Gibco, US) and incubated at 5% CO_2, 37 °C. Cells were trypsinized, centrifuged and resuspended in fresh culture media after they reach confluency. Afterwards, cells were seeded on substrates at 2×10^3 cells per cm^2 and incubated. Cells were examined at 16, 24, 44 and 51 h after culture.

To further probe the effect of cell–cell contacts in cell alignment regulation, cells were treated with 20 μM blebbistatin (Sigma Aldrich, US) to partially inhibit cell–cell adhesion junctions. Blebbistatin was prepared in dimethyl sulfoxide (Thermo Fisher Scientific, US) and diluted with culture medium. The drug treated cells were incubated for 4 h prior to analysis to ensure the effect of inhibition.

Fluorescence staining

Cell nuclei and F-actin were stained with DAPI (Sigma Aldrich, US) and rhodamine phalloidin (Invitrogen, US) in the dark, respectively. Briefly, cell culture medium was removed and 4% formaldehyde (Invitrogen, US) was added to Petri dishes at room temperature for 15 min to fix the cells. Then the cells were permeated with 0.5% Triton X-100 solution (Invitrogen, US) at room temperature for another 15 min. Afterwards the cells were blocked with 3% BSA (Invitrogen, US) at room temperature for 1 h. The cells were then stained with 5 μg ml^{-1} of rhodamine phalloidin (Molecular Probes, US) and incubated for 1 h at room temperature with F-actin. Afterwards, the cells were stained with 300 nM

4′,6-diamidino-2-phenylindole (Molecular Probes, US) for 5 min at room temperature and mounted for imaging.

Cell shape and alignment

Quantitative analysis was implemented by outlining the contour of every identifiable cell manually using Fiji/ImageJ (National Institutes of Health, US). For an individual cell, the cell aspect ratio was used to characterize the cell shape. The cell aspect ratio is defined as the ration of cell length to cell width (defined by the length of long and short axes of cellular best fit ellipse, respectively). The cell center was defined as the center of the ellipse. The groove direction was defined as the tangential direction of the point on groove sidewalls that was nearest to the cell center. The cell alignment angle was calculated as the angle between the cellular long axis and the groove direction.

Modelling of mechanical stress of patterned cell sheets

Mechanical stress distribution of a patterned cell sheet was analysed by a finite element method.[23,25,26] The circular and elliptical ring-shaped finite element models consist of a 5 μm thick contractile top layer to simulate the cell layer and a 1 μm thick passive bottom layer with a fixed bottom surface to simulate the extracellular matrix layer. Other dimensions of the model were prescribed elsewhere. A thermal strain induced by dropping the temperature by 5 K on the top layer was imported to simulate cell contraction. The thermal conductivity and the coefficient of expansion of the top layer were defined as 10 W m^{-1} K^{-1} and 0.05 K^{-1}, respectively. Both the top and the bottom layers were treated as isotropic elastic materials with a value of 0.499 for Poisson's ratio and 500 and 100 Pa for the Young's modulus, respectively. The elemental maximum principal stress of the top layer was reported as maximum intercellular principal stress. Meshes of different sizes (varied from 1–10 μm) were generated to confirm the convergence of the result.

Data processing and statistical analysis

All images were taken using a Leica DMI3000B (Leica, Germany) microscope in phase contrast and fluorescence mode and processed using MATLAB (MathWorks, US) and Fiji/ImageJ image processing softwares and associated plugins (National Institutes of Health, US). Three randomly chosen regions for each substrate were imaged. One-way analysis of variance (ANOVA) followed by Turkey's *post hoc* analysis for pairwise mean comparisons was performed to determine the statistical differences between or within each group unless otherwise mentioned. The statistical significance was defined as $*p < 0.05$, $**p < 0.01$, and $***p < 0.005$. Statistical analysis was implemented with and statistical graphs were drawn using Origin (OriginLab, US).

Results

Photolithography fabricated ring-shaped composite polymers and glass substrates

Concentric circular and elliptical groove patterned substrates were fabricated by standard photolithography procedures (Fig. 1A–D). Circular substrates consist of 100, 150 and 200 μm wide groove spacing of 100, 150 and 200 μm apart respectively. Elliptical substrates consist of 50 to 100, 75 to 150 and 100 to 200 μm wide groove spacing of 50, 75 and 100 μm apart in the short axis direction and 100, 150 and 200 μm apart in the long axis direction, respectively (Fig. 1E–H). Both circular and elliptical substrates were fabricated with two groove depths of 1.7 and 0.4 μm. All cells were cultured on substrates with 1.7 μm deep grooves with a flat substrate as control unless otherwise mentioned. Cellular morphological and alignment parameters are illustrated in Fig. 1I.

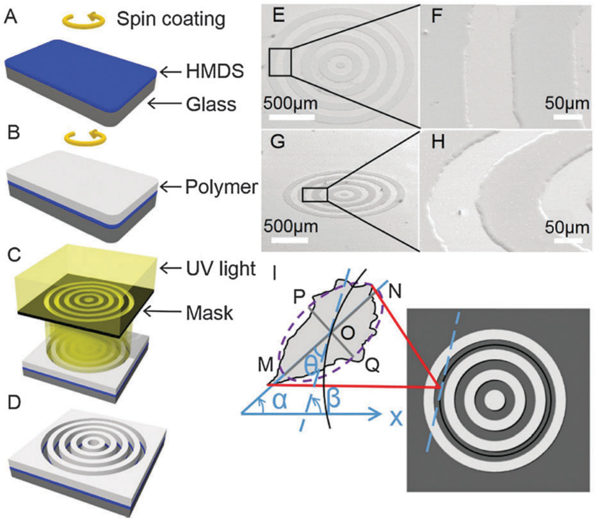

Fig. 1 Substrate fabrication and definition of the cell shape and alignment. (A–D) Standard lithography procedures to fabricate the substrate with circular and elliptical constraints. Linear constraints were drawn as examples to illustrate the procedures. SEM images showed the fabricated circular (E and F) and elliptical (G and H) substrates with 150 μm wide concentric circular groove spacing of 150 μm apart. (I) Diagram illustrating the cell aspect ratio and cell alignment angle (θ) the on patterned substrate. The ellipse is the best fitted ellipse of the cell shape. The angle of inclination of the long axis and the groove direction are represented by α and β, respectively. The scale bar is 500 μm in (E) and (G) and 50 μm in (F) and (H).

Cell distribution on ring-shaped composite substrates

Distributions of cells cultured on concentric circular and elliptical patterned substrates were characterized by showing the number of cells proliferated in grooves as a percentage of total cells (*G* for short). Cells crossing groove sidewalls were defined as cells on ridges (Fig. 2A). On circular substrates, cells showed a clear preference for proliferation in grooves. Percentages of cells in grooves of substrates with all dimensions increased and reached their maximum after 44 h of culture ($G = 0.88 \pm 0.07$, 0.95 ± 0.07 and 0.83 ± 0.02 for 100, 150 and 200 μm substrates respectively) (Fig. 2B). Cells were separated and formed several circular patterns, no closed pattern though, with regard to substrate patterns (Fig. 2). Then the percentage of cells in grooves decreased but no significant difference occurred at 51 h of culture. On elliptical substrates, cell distribution exhibited similar trends (Fig. 2B). The turning point of the percentage

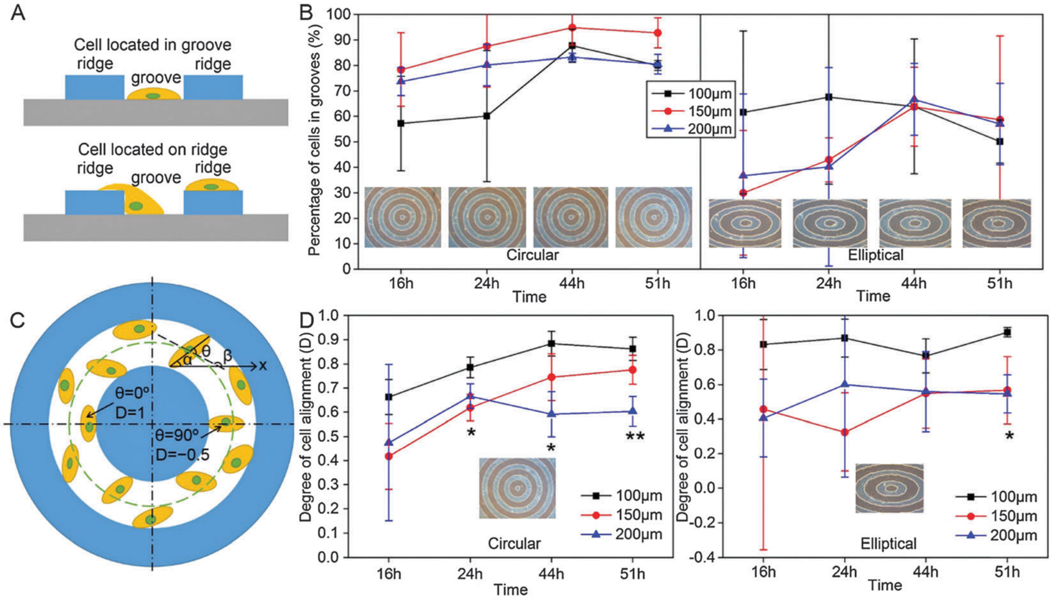

Fig. 2 Cell distribution and alignment on substrates patterned with curved constraints. (A) Diagram illustrating the definition of the cell located in the groove or on the ridge. (B) Percentage of cells located in grooves of concentric circular and elliptical patterned substrates as a function of time. Inset figures are phase contrast images at different times. (C) Diagram illustrating the cell alignment angle and the alignment degree. The cell angle and the groove direction are shown as α and β. The cell alignment angle is shown as θ. (D) Alignment degree of cells in grooves of concentric circular and elliptical substrates as a function of time. All parameters were calculated and shown as mean ± SD.

of cells in 150 and 200 μm wide grooves occurred at 44 h of culture while the percentage of cells in 100 μm wide grooves began to decrease at 24 h of culture. No statistically significant difference was found among all groove dimensions at each examined time point ($p > 0.1$ for all cases).

Cell alignment on ring-shaped composite substrates

With previous definitions (Fig. 1I), the cell alignment angle (θ) can be calculated as

$$\theta = \begin{cases} |\alpha - \beta|, \text{ if } |\alpha - \beta| \leq 90^\circ \\ 180^\circ - |\alpha - \beta|, \text{ else} \end{cases}$$

For the purpose of obtaining hollow cell patterns with well oriented cells, we only focused on cells that were proliferated in grooves. The cell alignment degree (D) was calculated by using the average value of the second order Legendre polynomial of the cell alignment angle (θ), an approach commonly employed when characterizing the preferred directionality in liquid crystals.[27,28]

$$D = \left\langle \frac{3\cos^2\theta - 1}{2} \right\rangle$$

D will approach 1 if θ approaches 0 degree, which means that there is a strong degree of correlation between the cell angle and the groove direction. D will approach 0 if θ is randomly distributed, which means that cells are randomly oriented. Moreover, D will approach -0.5 if θ approaches 90 degrees, which means that cells orient perpendicular to the groove direction (Fig. 2C). On circular substrates, the cell alignment degree increased from cell seeding to 44 h after cell culture for 100 and 150 μm substrates (Fig. 2D). After 51 h of culture, the alignment degree of the cell in 100 ($D = 0.86 \pm 0.05$) and 150 μm ($D = 0.78 \pm 0.06$) wide grooves were significantly higher than that of cells in 200 μm wide grooves ($D = 0.63 \pm 0.03$) ($p < 0.005$ in both cases). For cells proliferated on concentric elliptical patterned substrates, the alignment degree of cells in 100 μm wide grooves ($D = 0.90 \pm 0.03$) was found to be significantly higher than that of cells in 150 and 200 μm wide grooves after 51 h of culture ($D = 0.57 \pm 0.2$ and 0.55 ± 0.12, $p = 0.048$ and 0.044 respectively). In addition, cell alignment angles were more concentrated for cells on all substrates at 51 h of culture because standard deviations of cell alignment degrees decreased as culture time increased (Fig. 2D).

In order to study the influence of curvature on cell alignment, we examined the cell alignment degree on concentric circular patterned substrates. Each ring-shaped groove composes two circular sidewalls with different radii. For an individual cell that proliferates in such a groove, cell alignment is supposed to be more closely affected by one groove sidewall if that wall is nearer to the cell center than the other one. Thus cells proliferated on a certain substrate can be divided into several groups, each is characterized by one radius of curvature (R_c) of groove sidewalls (Fig. 3A and B and Fig. S1, ESI†). Generally, relative frequency declined as the cell alignment angle increased for all curvatures (Fig. 3C–E). One-way ANOVA of the cell alignment degree of different groove curvatures showed no significant difference when groove widths are 100 and 150 μm (Fig. 3F, $p = 0.66$ and 0.23 respectively). For the 200 μm substrate, pairwise comparison of the cell alignment degree of different groove curvatures

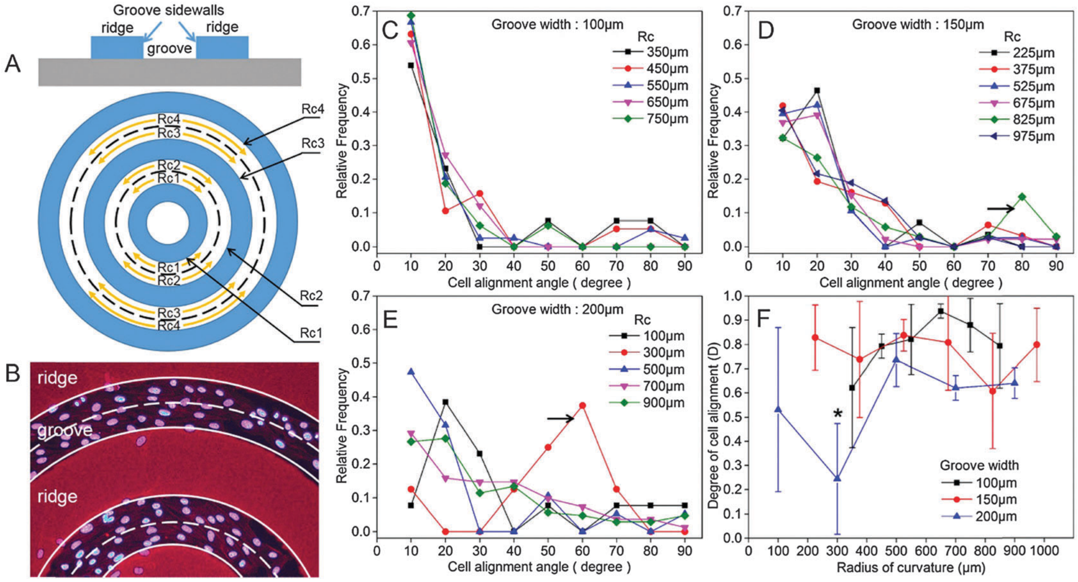

Fig. 3 Cell alignment angle distribution and the cell alignment degree over radii of groove curvatures on circular patterned substrates at 51 h of culture. (A) Diagram illustrating groove sidewalls (top) and groove regions divided by the distance to groove sidewalls (bottom). Groove sidewalls were represented by radii of their curvatures from Rc1 to Rc4. Points on each dashed line are equidistant from both groove sidewalls. Cells located in between Rc1 and dashed line were supposed to be affected more by Rc1 and so on. (B) Fluorescence image of myoblast nuclei (blue) and polymeric ridges (red) on the 150 μm patterned substrate. Plots show the distribution of the cell alignment angle of different curvatures of grooves with widths of (C) 100 μm, (D) 150 μm and (E) 200 μm. (F) Degree of cell alignment (*D*) changed with groove curvatures on 100, 150 and 200 μm circular patterned substrates. If there is a high degree of parallel or perpendicular alignment between the cell and the groove direction, *D* will approach 1 or 0, respectively.

showed no significant difference ($p > 0.33$ for all cases) except when the alignment degree of the groove curvature whose R_c is 300 μm is compared to those whose R_c values are 500 and 700 μm (Fig. 3E and F, $p = 0.016$ and 0.048 respectively).

The cell alignment degree of circular and their corresponding elliptical substrates was also compared to evaluate the influence of parallelism of constraint boundaries on cell orientation. There was no statistically difference in the cell alignment degree between parallel and unparallel constraints (Fig. 4A and B).

Cell and nuclear shape on ring-shaped composite substrates

The cell and nuclear aspect ratios were used to characterize their shape. By 51 h time points, the cell aspect ratio was significantly higher on 100 μm substrates than on 150 and 200 μm substrates (Fig. S2, ESI,† $p < 0.005$ for both cases). At the same time, the cell aspect ratio was independent of the curvatures of constraints (Fig. 4C). Moreover, there was no statistically difference in the cell aspect ratio between circular and their corresponding elliptical substrates with parallel and unparallel boundaries, respectively (Fig. 4D). Although nuclear aspect ratios were higher on patterned composite substrates than on flat glass substrates, there was no statistically difference in that between all circular and their corresponding elliptical substrates and between all circular and elliptical substrates with different dimensions. However, the significant level of circular and their corresponding elliptical substrates compared to flat substrates differs. Nuclei on circular substrates elongated more significantly than on their corresponding elliptical substrates (Fig. 5).

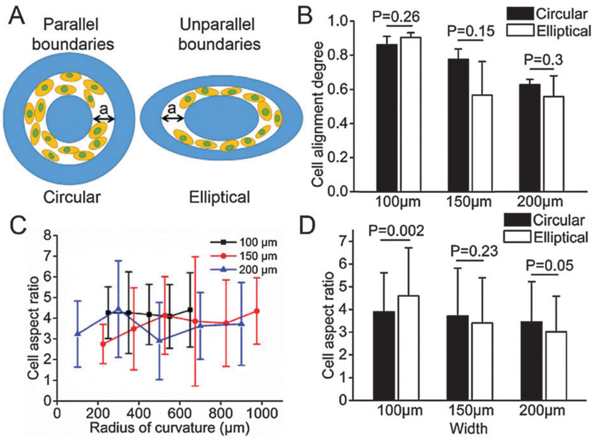

Fig. 4 Influence of parallelism of boundaries of constraints on the cell alignment and the cell aspect ratio. (A) Diagram illustrating constraints with parallel and unparallel boundaries. Parallel constraints provide fixed widths while unparallel constraints provide varied width that is narrower than the former. Scale bars = 40 μm. (B) Comparisons of the cell alignment degree between circular constraints with widths of 100, 150 and 200 μm and their corresponding elliptical constraints with widths of 50 to 100, 75 to 150 and 100 to 200 μm. (C) Influence of the curvature on the cell aspect ratio. (D) Comparisons of the cell aspect ratio between circular and elliptical constraints.

Discussion

Distribution of myoblasts is a result of complex cellular response to combinational guidance features

It has been proved that stiffness is a strong tool to pattern cells even superior to the patterned matrix.[10] Spatial stiffness variations

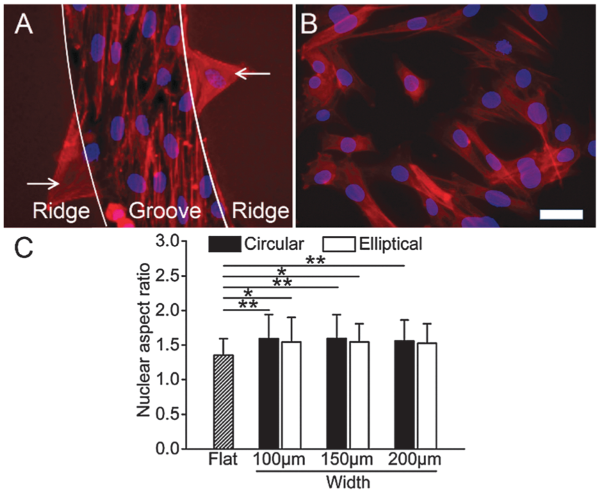

Fig. 5 Influence of substrate patterns on the nuclear aspect ratio. (A) Fluorescence images of F-actin (red) and nuclei (blue) of cells on the 150 μm circular composite and flat glass substrate (B) after 51 h of culture. Polymeric ridges were also imaged and shown in red. (C) Comparisons of the nuclear aspect ratio of different substrate patterns. Scale bar is 40 μm.

can induce durotaxis and form cell patterns.[29] Here, the stiffness difference of polymeric ridges and glass grooves could lead myoblasts to migration towards stiff grooves other than soft ridges. Moreover, cells can sense the effective stiffness of rigid substrates that are not in direct cellular contact when they are cultured on a thin polymeric film affixed to a rigid substrate.[30–33] Therefore we could expect that myoblasts were randomly distributed when a polymeric film was thin enough so that myoblasts were unable to sense the difference in the effective stiffness between ridge and groove surfaces because stiffness of glass could be transferred to the ridge surface. To test our hypothesis, we first confirmed that the collagen was uniformly coated on glass and the photoresist with the same thickness. Then we performed nanoindentation on the surface of collagen coated glass, and 0.4 μm and 1.7 μm thick photoresists on glass, respectively. The results showed that the 0.4 μm photoresist is as stiff as glass while stiffer than the 1.7 μm photoresist (Fig. S6, ESI†). Afterwards, we cultured myoblasts on substrates with the same patterns but 400 nm deep grooves. No cell pattern was formed and no organization was observed as expected even at 72 h after culture (Fig. S3, ESI†). To exclude a mere effect of the substrate grooved pattern on cell distribution, we cultured cells on the grooved glass substrate (without a polymer) with the same pattern and the groove depth (1.7 μm) as the composite substrate previously presented. Myoblasts showed no preference for going inside and proliferating in the grooves after 72 h of culture (Fig. S4, ESI†). To further exclude the effect of collagen, we cultured cells on collagen coated and non-coated substrates. Although cells were more elongated on collagen coated than non-coated substrates, a similar distribution was observed on both substrates (Fig. S5, ESI†). Therefore, we confirmed that stiffness played an important role in cell distribution because the surface properties of the material do not vary but effective stiffness varies due to polymer film thinning. Additionally, cells located on plateau ridges were less elongated and more spread than those located in grooves (Fig. 5A). This infers that the difference of surface chemistry between grooves and ridges also might contribute to cell distribution through formation of different collagen crosslinking densities. These cues indicate that the distribution of myoblasts could be a result of complex cellular response to combinational guidance features.

Effects of ring-shaped composite substrates on cell alignment

Curvature of the curved constraint has no influence on cell alignment. It is found that cell–cell interaction acts as the communication pathway for passing microenvironment information between neighbouring cells to induce the direction of cell growth and migration.[34–36] Therefore cell contact guidance can be induced not only by subcellular scale constraints, but also by supracellular scale constraints as well. In addition, the diameter of the muscle layer of hollow tissues and organs *in vivo* varied from microns to centimetres. Recently, the influence of supracellular scale curvature on cell mechanics was studied on the surface of cylinders or on the inner surface of tubular structures.[2,37–39] But the influence of curvature on myoblast alignment has not been quantitatively elucidated. In this paper we cultured myoblasts on both concentric circular and elliptical substrates. To get rid of the influence of groove width, we mostly focused on the cell alignment of the concentric circular substrate that composes grooves with a fixed width but varied curvatures. Statistical analysis demonstrated that curvatures had no significant influence on cell alignment for 100 and 150 μm substrates, which means that curved constraints can also induce contact guidance effectively (Fig. 3F). As for the 200 μm substrate, it is worth noting that pairwise comparison of the cell alignment degree of all radii of curvatures higher and lower than 300 μm showed no significant influence on cell alignment ($p = 0.40$). Therefore we believe the significant decline of the cell alignment degree at 300 μm was caused by the lack of cell–cell contact at some local regions near the groove sidewall which led to insufficient cell–cell interactions to pass the boundary information of constraints to the neighbouring cells. Overall, the results suggest that myoblasts can orient along curved constraints independent of their curvatures.

Dimensions of the curved constraint significantly affects cell alignment. Although the effects of the groove width on myoblast alignment, morphology and differentiation have been investigated substantially, few studies have investigated the role which width plays in curved constraints. Recently, osteoblasts were observed to orient along the groove direction when cultured on concentric circular grooves with the width well below 100 μm. Percentages of the cell alignment angle smaller than 15 degrees decreased from 75% to 20% when the groove width increased from 7.5 to 96.2 μm.[40] In contrast, myoblasts were highly oriented along the groove direction on substrates with the groove width beyond 100 μm here which is in favour of tissue scaffold fabrication because mesoscale features can be fabricated more easily. In addition, cell–cell contacts weakened as the groove width increased because more space is available for cells to proliferate and migrate, which is responsible for the phenomenon that better oriented cells were observed in narrower grooves in our experiment (Fig. 2D).

Parallelism of boundaries of the curved constraint significantly affects cell alignment. Concentric circular substrates can serve as the control group of elliptical substrates because cell alignment is not affected by the mechanical constraint curvature as we have demonstrated, consistent with a previous study that align myoblasts on matrix constraints.[23] Since substrate dimensions instead of curvature significantly affect cell alignment as stated above, it is expected that cells were better oriented along groove directions on elliptical substrates because groove widths of the 100, 150 and 200 μm patterned substrates actually vary from 50 to 100 μm, 75 to 150 μm and 100 to 200 μm respectively. However, there was no statistically significant difference in the cell alignment degree between circular and their corresponding elliptical substrates ($p > 0.1$ for all cases) (Fig. 2D). It is worth noting that concentric elliptical grooves here presented do not possess parallel elliptical groove sidewalls indeed (Fig. S7, ESI†). Therefore, these results infer that parallelism of constraints also plays an important role in cell alignment regulation. Constraints with parallel boundaries can favourably align cells with boundary directions, thus resulting in a higher cell alignment degree than the constraint with unparallel boundaries.

The mechanisms underlying the influences of dimensions, curvatures and parallelism of boundaries of constraints on cell alignment. We observed that before cells filled the surface of the grooves, they exhibited a low degree of alignment. Only cells proliferated near groove sidewalls oriented along groove directions and cells proliferated in the middle region of the grooves were randomly aligned. However, when cells sufficiently filled the surface of the grooves, which led to high level cell–cell contacts, they started to realign along groove directions (Fig. S8, ESI†). It has been proved that cell–cell contacts can transmit intercellular normal and shear stresses and eventually align the long axis of the cell along the orientation of local minimal intercellular shear stress, which is equivalent to the orientation of maximum principal stress.[35,41] Therefore, we assumed that the orientation of maximum intercellular principal stress depends not only on curvatures but also on dimensions and parallelism of the curved constraint. To test our hypothesis, we inspected the orientation of maximum intercellular principal stress exerted by adjacent cells under the influence of curved parallel and unparallel constraints with varied dimensions and curvatures. Finite element analysis was implemented to evaluate the bias angle θ_S of the orientation of maximum principal stress with respect to constraint directions (Fig. 6).

To assess the mechanisms underlying the influence of dimensions and curvatures of circular ring-shaped constraints on cell alignment, we built circular ring-shaped finite element models with a fixed inner diameter and varied distances between the inner and outer boundaries and with varied inner diameters and a fixed distance of 150 μm between the inner and outer boundaries, respectively. Other details of the models have been prescribed above. We found that θ_S enlarges significantly as the distance between the inner and outer boundaries increases ($p < 0.001$, Fig. 6C). This result reconfirms our experimental results which concluded that myoblasts orient along the directions of boundaries better in narrower constraints than in wider ones and reveals that intercellular stresses are the driven forces that align myoblasts along curved constraints. Additionally, the deviation of θ_S also extends as the width of the constraint increases. The color-coded orientation maps in Fig. 6C show that θ_S enlarges as the distance between meshed elements that simulates cells and boundaries of the constraint increases and reaches its maximum in the middle regions between inner and outer boundaries of the constraint with a given width. Previous studies have observed that cell alignment with respect to the direction of the constraint boundary depends on the cellular distance from the boundaries.[42,43] Our result provides this phenomenon a theoretical interpretation and emphasizes the vital role that intercellular forces play in inducing cell alignment.

To explore the mechanisms underlying the influence of the curvature of circular ring-shaped constraints on cell orientation, we fixed widths of ring-shaped constraints at 150 μm while decreased curvatures of boundaries of constraints. We found homogeneous patterns of color-coded maps of θ_S regardless of increasing radii of both boundaries ($p > 0.1$, Fig. 6D). This indicates that orientation of maximum intercellular principal stress, which is equivalent to cell orientation as stated above, is independent of the curvature of curved constraints, consistent with our experimental results.

We then explored the influence of parallelism on θ_S. To simplify the model but not lose generality, we built an unparallel elliptical ring-shaped finite element model with the corresponding parallel elliptical model as control. The in plane dimensions of the parallel and unparallel models were described above. Although the width of the unparallel model is smaller than that of the parallel model, the finite element result of θ_S showed no significant difference ($p > 0.1$, Fig. 6E). The simulation results are in conflict with our previous conclusions depicting that narrow curved constraints are superior to wide ones. Instead, it demonstrates the role that parallelism of boundaries of constraints plays in cell alignment guidance, which agrees with our experimental results. To verify that they are unparallel boundaries of constraints that disorders orientation of maximum principal stress, we also evaluated the degree of parallelism of the elliptical ring-shaped constraint through calculating the angle (θ_P) between the direction of inner and outer boundaries with respect to locations across the entire constraint (Fig. 6B). We found that the most unparallel regions between inner and outer boundaries locate around both ends of the long axis, consistent with the locations of the most disordered orientation of maximum principal stress in our finite analysis results. The same scenario appears in regions near both ends of the short axis, where highly ordered maximum principal stress was observed with parallel boundaries (Fig. 6E and F). These results infer that there is a strong correlation between parallelism of boundaries of the constraint and cell orientation. Constraints possessing parallel boundaries are more conducive to inducing cell alignment,

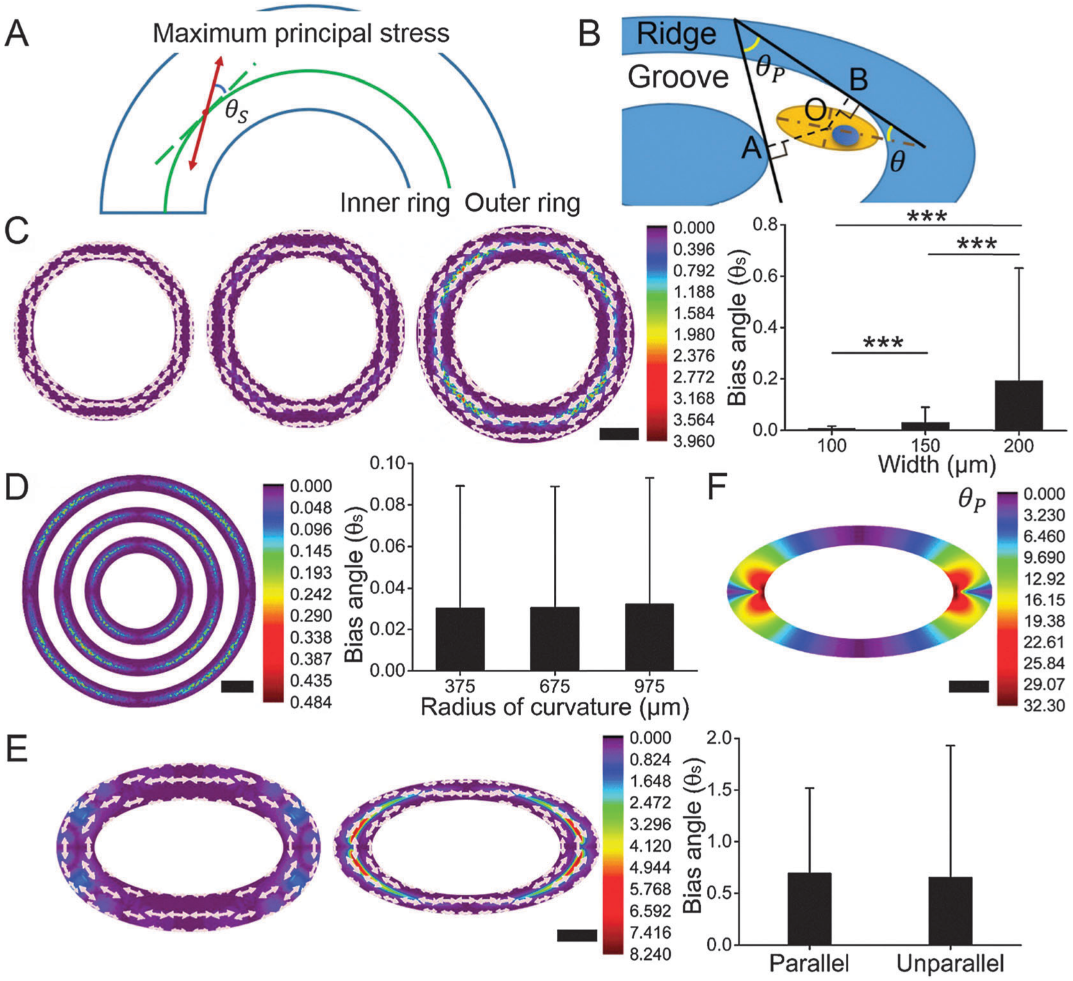

Fig. 6 Finite element results of orientation maps of intercellular maximum principal stresses with respect to directions of constraint boundaries and parallelism maps of elliptical ring-shaped constraints with varied width (unparallel boundaries). Overlain upon these maps are white arrows depicting vectors of maximum principal stresses. (A) The bias angle of maximum principal stress (the red line with arrows) was defined as θ_S based on the deviation from the circumferential direction (green dashed line). (B) The degree of parallelism of inner and outer boundaries was defined as θ_P based on the interangle between tangent lines (black solid lines) of the nearest points on inner (point A) and outer (point B) boundaries with respect to the cell center (point O). (C) Left panel shows color-coded maps of θ_S of circular ring-shaped models with an inner diameter of 750 μm and a distance of 100 (left), 150 (middle) and 200 μm (right) between the inner and outer boundaries. The right panel shows θ_S of the corresponding circular ring-shaped models with different widths. (D) The left panel shows color-coded maps of θ_S of circular ring-shaped models with inner diameters of 750 (inner), 1350 (middle) and 1950 μm (outer) and a distance of 150 μm between the inner and outer boundaries. The right panel shows θ_S of the corresponding models with different curvatures. (E) The left panel shows color-coded maps of θ_S of elliptical ring-shaped models with inner long and short axes of 750 and 375 μm and a distance of 150 μm between the inner and outer boundaries (left) and with inner ellipse of the same dimensions as the inner ellipse of the former constraints and outer long and short axes of 1050 and 525 μm (right). The right panel shows θ_S of the corresponding elliptical ring-shaped models with parallel and unparallel boundaries. Student's *t* test was performed to determine the difference between the two groups. (F) Color-coded parallelism maps of θ_P of elliptical ring-shaped constraints. The scale bar is 200 μm in (C), (E) and (F) and 400 μm in (D).

providing guidance in the design of scaffolds for noncircular hollow tissue engineering.

To confirm the relationship of cell alignment with respect to cooperative intercellular forces, we performed an drug test experiment to partially inhibit cell–cell connections through treating high level contacted cells with 20 μM blebbistatin.[44,45] Cell alignment angles with respect to groove directions were calculated. The results showed that cells were highly aligned along groove directions with over 70% cells aligned within 20 degrees of groove directions before drug treatment for both circular and elliptical substrates. However, cells began to randomly orient which resulted in the same parameter being decreased to below 40% when cell–cell connections were inhibited (Fig. 7).

Taken together our experimental, simulation and drug test results, we can conclude that cooperative intercellular forces exerted by adjacent cells are the driving forces that propel cells to reoriente themselves to align along the directions of boundaries of curved constraints. By combining the effects of the topographic, mechanical and surface chemistry properties

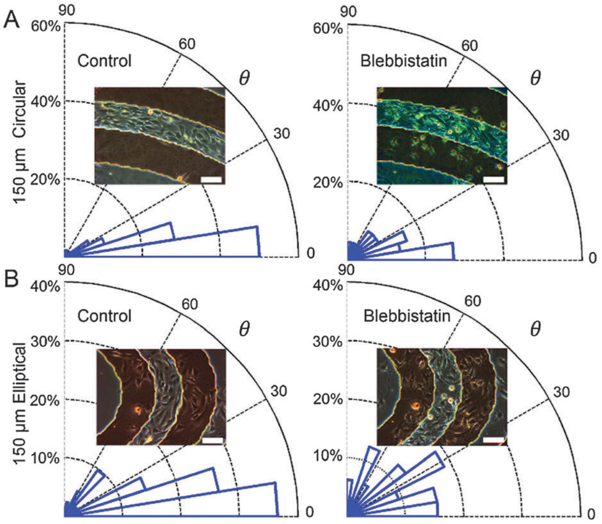

Fig. 7 Effect of blebbistatin induced cell–cell contact inhibition on the cell alignment angle distribution. The alignment angle (θ) of cells on 150 μm circular (A) and elliptical (B) were calculated before and 4 h after blebbistatin treatment, respectively. Insets were phase contrast images of cells at the same position of the substrate before and after drug treatment. Scale bar is 100 μm.

of boundaries on cell organization, our substrates eliminated the impeditive effect of cell chirality excreted on the formation of the end-to-end cellular sequence with respect to cell patterns when cells were seeded on the patterned matrix.

Although glass is not an implantable material, our model showed that the mechanisms of how dimensions, curvature and parallelism affect cellular organization are basically independent of the substrate material. The model only set line for stiffness of the material so that cells cannot substantially deform the substrate. Materials satisfying the condition, whether they are porous, biocompatible and biodegradable or not, can utilize our model. Therefore, we believe that design rules derived from the *in vitro* studies reported here can be applied when designing scaffolds utilizing implantable materials to improve sphincter-like tissue regeneration strategies *in vivo*.

Effects of ring-shaped composite substrates on the myoblast shape

The altered cell and nuclear shape play an important role in the differentiation of myotubes.[46,47] Based on our observations that cells were more elongated in circular narrow constraints than in wide ones and that curvatures showed no influence on the cell aspect ratio, we can preliminary count that substrate dimensions dominate the cell aspect ratio. However, there was no statistically difference in the cell aspect ratio between circular and their corresponding elliptical substrates whose dimensions are narrower than circular ones except 100 μm substrates (Fig. 4D). Therefore we can conclude that parallelism of constraint boundaries also significantly affects cell aspect ratios. Additionally, cytoplasmic actin filaments are essential features in the modulation of the nuclear shape and function. It has been proved that there exists a mechanistic coordination between the cell and nuclear shape.[48,49] Consequently, the nuclear aspect ratio obeys the same rules set by dimensions and parallelism of the constraint for the cell aspect ratio.

Conclusions

This study revealed a simple method to engineer circular and elliptical ring-shaped myoblast patterns and maximize the corresponding cell alignment simultaneously. Different from previous methods that pattern cells with patterned matrices and stiffness fabricated through microcontact printing and soft lithography, the method presented is mold-free. We demonstrated that myoblasts are able to orient along our substrates with width of several folds beyond the typical individual cell scale even when the constraint is curved. This result is important because it means that we can engineer large-scale ring-shaped tissue in a cheap way since supracellular scale constraints can be fabricated easier than subcellular ones. We also proved, both experimentally and theoretically, that myoblasts track the direction of curved constraints better in narrower constraints than in wider ones. Therefore, compromises should be made between the degree of cell alignment and the cost of the fabrication of scaffolds when we design the dimensions of scaffolds. Interestingly, as a typical character of curved constraints, curvature showed no influence on myoblast alignment. Additionally, we also investigated the influence of parallelism of the constraints on cell behaviour and demonstrated that constraints with parallel boundaries are prone to induce contact guidance better than unparallel ones. To the best of our knowledge, this is the first time that the influence of parallelism of constraints on cells' behaviour is investigated. In fact, parallelism of the curved constraint is one character that we cannot disregard in the design of the substrate or scaffold for noncircular ring-shaped tissue engineering. We concluded that narrow and parallel features are key parameters that should be considered in the design of curved constraints in order to maximize cell alignment for ring-shaped myotube generation. These design rules can be incorporated into the surface of scaffolds utilizing implantable materials for urethral sphincter engineering. Finally, although rigid materials such as glass are not ideal candidates for optimal myotube differentiation, our substrates hold the potential to serve as a compliant bottom layer of glass-attached myotubes with tissue like stiffness for cell-on-cell sphincter-like tissue engineering,[50,51] which can potentially benefit the treatment of stress urinary incontinence.

Acknowledgements

We appreciate Dr Zhen Guo and the Laboratory of Cellular Dynamics at the University of Science and Technology of China for their kind support. This work is financially supported by the Fundamental Research Funds for the Central Universities. This work was partially carried out at the USTC Center for Micro and Nanoscale Research and Fabrication.

References

1 A. Stenzl and K. D. Sievert, *Eur. Urol.*, 2007, **52**, 1574–1575.

2 F. A. Zouraq, M. Stölting and D. Eberli, *Skeletal Muscle Regeneration for Clinical Application*, 2013.

3 Y. Shi, Y. Li, J. Liu and Y. Zhang, *Cell Therapy and Muscle Regeneration: Skeletal Myogenic Differentiation of Urine-Derived Stem Cells for Potential Use in Treatment of Urinary Incontinence*, 2013.

4 D. Huh, Y. S. Torisawa, G. A. Hamilton, H. J. Kim and D. E. Ingber, *Lab Chip*, 2012, **12**, 2156–2164.

5 F. Khan, M. Tanaka and S. R. Ahmad, *J. Mater. Chem. B*, 2015, **3**, 8224–8249.

6 M. Verhulsel, M. Vignes, S. Descroix, L. Malaquin, D. M. Vignjevic and J. L. Viovy, *Biomaterials*, 2014, **35**, 1816–1832.

7 X. Yao, R. Peng and J. D. Ding, *Adv. Mater.*, 2013, **25**, 5257–5286.

8 C. A. DeForest and D. A. Tirrell, *Nat. Mater.*, 2015, **14**, 523–531.

9 M. V. Tsurkan, R. Wetzel, H. R. Pérez-Hernández, K. Chwalek, A. Kozlova, U. Freudenberg, G. Kempermann, Y. Zhang, A. F. Lasagni and C. Werner, *Adv. Healthcare Mater.*, 2015, **4**, 516–521.

10 Y. S. Choi, L. G. Vincent, A. R. Lee, K. C. Kretchmer, S. Chirasatitsin, M. K. Dobke and A. J. Engler, *Biomaterials*, 2012, **33**, 6943–6951.

11 A. Higuchi, Q. D. Ling, Y. Chang, S. T. Hsu and A. Umezawa, *Chem. Rev.*, 2013, **113**, 3297–3328.

12 J. L. Charest, M. T. Eliason, A. J. Garcia and W. P. King, *Biomaterials*, 2006, **27**, 2487–2494.

13 H. Y. Hsieh, G. Camci-Unal, T. W. Huang, R. Liao, T. J. Chen, A. Paul, F. G. Tseng and A. Khademhosseini, *Lab Chip*, 2014, **14**, 482–493.

14 C. T. Ho, R. Z. Lin, R. J. Chen, C. K. Chin, S. E. Gong, H. Y. Chang, H. L. Peng, L. Hsu, T. R. Yew, S. F. Chang and C. H. Liu, *Lab Chip*, 2013, **13**, 3578–3587.

15 A. M. Ross, Z. Jiang, M. Bastmeyer and J. Lahann, *Small*, 2012, **8**, 336–355.

16 L. Altomare, N. Gadegaard, L. Visai, M. C. Tanzi and S. Fare, *Acta Biomater.*, 2010, **6**, 1948–1957.

17 C. L. Gilchrist, D. S. Ruch, D. Little and F. Guilak, *Biomaterials*, 2014, **35**, 10015–10024.

18 Y. M. Wang, H. G. Shi, J. Qiao, Y. Tian, M. Wu, W. Zhang, Y. Lin, Z. W. Niu and Y. Huang, *ACS Appl. Mater. Interfaces*, 2014, **6**, 2958–2962.

19 B. Yuan, Y. Jin, Y. Sun, D. Wang, J. S. Sun, Z. Wang, W. Zhang and X. Y. Jiang, *Adv. Mater.*, 2012, **24**, 890–896.

20 J. S. Choi, Y. Piao and T. S. Seo, *Biomaterials*, 2014, **35**, 63–70.

21 M. T. McClendon and S. I. Stupp, *Biomaterials*, 2012, **33**, 5713–5722.

22 L. Q. Wan, K. Ronaldson, M. Park, G. Taylor, Y. Zhang, J. M. Gimble and G. Vunjak-Novakovic, *Proc. Natl. Acad. Sci. U. S. A.*, 2011, **108**, 12295–12300.

23 P. Bajaj, B. Reddy, L. Millet, C. N. Wei, P. Zorlutuna, G. Bao and R. Bashir, *Integr. Biol.*, 2011, **3**, 897–909.

24 Y. H. Tee, T. Shemesh, V. Thiagarajan, R. F. Hariadi, K. L. Anderson, C. Page, N. Volkmann, D. Hanein, S. Sivaramakrishnan, M. M. Kozlov and A. D. Bershadsky, *Nat. Cell Biol.*, 2015, **17**, 445–457.

25 C. M. Nelson, R. P. Jean, J. L. Tan, W. F. Liu, N. J. Sniadecki, A. A. Spector and C. S. Chen, *Proc. Natl. Acad. Sci. U. S. A.*, 2005, **102**, 11594–11599.

26 B. Li, F. Li, K. M. Puskar and J. H. Wang, *J. Biomech.*, 2009, **42**, 1622–1627.

27 A. Leclerc, D. Tremblay, S. Hadjiantoniou, N. V. Bukoreshtliev, J. L. Rogowski, M. Godin and A. E. Pelling, *Biomaterials*, 2013, **34**, 8097–8104.

28 W. F. Zheng and X. Y. Jiang, *Colloids Surf., B*, 2014, **124**, 97–110.

29 T. H. Qazi, D. J. Mooney, M. Pumberger, S. Geissler and G. N. Duda, *Biomaterials*, 2015, **53**, 502–521.

30 A. Higuchi, Q. D. Ling, S. S. Kumar, Y. Chang, A. A. Alarfaj, M. A. Munusamy, K. Murugan, S. T. Hsu and A. Umezawa, *J. Mater. Chem. B*, 2015, **3**, 8032–8058.

31 B. Amnon, R. Karthikan, E. X. B. Andre' and E. D. Dennis, *J. Phys.: Condens. Matter*, 2010, **22**, 194116.

32 B. Oommen and K. J. Van Vliet, *Thin Solid Films*, 2006, **513**, 235–242.

33 I. T. Hoffecker, W. H. Guo and Y. L. Wang, *Lab Chip*, 2011, **11**, 3538–3544.

34 X. Trepat, M. R. Wasserman, T. E. Angelini, E. Millet, D. A. Weitz, J. P. Butler and J. J. Fredberg, *Nat. Phys.*, 2009, **5**, 426–430.

35 D. T. Tambe, C. C. Hardin, T. E. Angelini, K. Rajendran, C. Y. Park, X. Serra-Picamal, E. H. H. Zhou, M. H. Zaman, J. P. Butler, D. A. Weitz, J. J. Fredberg and X. Trepat, *Nat. Mater.*, 2011, **10**, 469–475.

36 S. R. K. Vedula, M. C. Leong, T. L. Lai, P. Hersen, A. J. Kabla, C. T. Lim and B. Ladoux, *Proc. Natl. Acad. Sci. U. S. A.*, 2012, **109**, 12974–12979.

37 A. Y. Hsiao, T. Okitsu, H. Onoe, M. Kiyosawa, H. Teramae, S. Iwanaga, T. Kazama, T. Matsumoto and S. Takeuchi, *PLoS One*, 2015, **10**, e0119010.

38 H. Kang do, S. M. Kim, B. Lee, H. Yoon and K. Y. Suh, *Analyst*, 2013, **138**, 6230–6242.

39 M. Junkin, S. L. Leung, S. Whitman, C. C. Gregorio and P. K. Wong, *J. Cell Sci.*, 2011, **124**, 4213–4220.

40 K. Wang, L. Cai, L. Zhang, J. Y. Dong and S. F. Wang, *Adv. Healthcare Mater.*, 2012, **1**, 292–301.

41 X. Trepat and J. J. Fredberg, *Trends Cell Biol.*, 2011, **21**, 638–646.

42 F. J. Segerer, F. Thuroff, A. P. Alberola, E. Frey and J. O. Radler, *Phys. Rev. Lett.*, 2015, **114**, 5.

43 S. J. He, C. L. Liu, X. J. Li, S. P. Ma, B. Huo and B. H. Ji, *Biophys. J.*, 2015, **109**, 489–500.

44 Z. Liu, J. L. Tan, D. M. Cohen, M. T. Yang, N. J. Sniadecki, S. A. Ruiz, C. M. Nelson and C. S. Chen, *Proc. Natl. Acad. Sci. U. S. A.*, 2010, **107**, 9944–9949.

45 M. Vicente-Manzanares, X. F. Ma, R. S. Adelstein and A. R. Horwitz, *Nat. Rev. Mol. Cell Biol.*, 2009, **10**, 778–790.

46 N. M. Rodriguez, R. A. Desai, B. Trappmann, B. M. Baker and C. S. Chen, *Langmuir*, 2014, **30**, 1327–1335.

47 L. Wang, Y. Wu, B. Guo and P. X. Ma, *ACS Nano*, 2015, **9**, 9167–9179.

48 M. Versaevel, T. Grevesse and S. Gabriele, *Nat. Commun.*, 2012, **3**, 671.

49 B. Chen, C. Co and C. C. Ho, *Biomaterials*, 2015, **67**, 129–136.

50 A. J. Engler, M. A. Griffin, S. Sen, C. G. Bonnetnann, H. L. Sweeney and D. E. Discher, *J. Cell Biol.*, 2004, **166**, 877–887.

51 D. E. Discher, P. Janmey and Y. L. Wang, *Science*, 2005, **310**, 1139–1143.